AFRL-AFOSR-JP-TR-2020-0014

Development of gamma' precipitation-strengthened W-free Co-base superalloys for gas turbine applications

Pyuck-Pa Choi
Korea Advanced Institute of Science and Technology
291 Daehak-ro, Yuseong-gu
Taejon, 305701
KR

10/07/2020
Final Report

Air Force Research Laboratory
Air Force Office of Scientific Research
Asian Office of Aerospace Research and Development
Unit 45002, APO AP 96338-5002

REPORT DOCUMENTATION PAGE

Form Approved
OMB No. 0704-0188

1. REPORT DATE *(DD-MM-YYYY)*	2. REPORT TYPE	3. DATES COVERED *(From - To)*
07-10-2020	Final	12 Jul 2016 to 11 Jul 2019

4. TITLE AND SUBTITLE
Development of gamma' precipitation-strengthened W-free Co-base superalloys for gas turbine applications

5a. CONTRACT NUMBER

5b. GRANT NUMBER
FA2386-16-1-4120

5c. PROGRAM ELEMENT NUMBER
61102F

6. AUTHOR(S)
Pyuck-Pa Choi

5d. PROJECT NUMBER

5e. TASK NUMBER

5f. WORK UNIT NUMBER

7. PERFORMING ORGANIZATION NAME(S) AND ADDRESS(ES)
Korea Advanced Institute of Science and Technology
291 Daehak-ro, Yuseong-gu
Taejon, 305701 KR

8. PERFORMING ORGANIZATION REPORT NUMBER

9. SPONSORING/MONITORING AGENCY NAME(S) AND ADDRESS(ES)
AOARD
UNIT 45002
APO AP 96338-5002

10. SPONSOR/MONITOR'S ACRONYM(S)
AFRL/AFOSR IOA

11. SPONSOR/MONITOR'S REPORT NUMBER(S)
AFRL-AFOSR-JP-TR-2020-0014

12. DISTRIBUTION/AVAILABILITY STATEMENT
A DISTRIBUTION UNLIMITED: PB Public Release

13. SUPPLEMENTARY NOTES

14. ABSTRACT
Superalloys strengthened by precipitates show outstanding high-temperature properties such as creep, oxidation, and hot corrosion resistance and are therefore the key materials in jet propulsion gas turbines. Recently, Co-based superalloys have attracted a great deal of attention for high-temperature applications. The interest in these new emerging alloys was triggered by the discovery of a / microstructure in the ternary Co-Al-W system, which is very similar to that of high-performance Ni-based superallloys. However, the main drawbacks of Co-Al-W-based superalloys are a limited phase stability and relatively low solvus temperatures (usually below ~ 1300 K). Moreover, they show a high density (about 10% higher than commercial Ni-alloys) due to the high amount of W (~ 10 at.%), which limits creep rupture life. The aim of this project is to develop new -strengthened alloys based on the Co-Ti system instead of Co -Al-W.

15. SUBJECT TERMS
Cobalt, Superalloy, Co, W-free, Tungsten-free, Gas turbine engine, Gamma, Gamma', Gamma prime

16. SECURITY CLASSIFICATION OF:			17. LIMITATION OF ABSTRACT	18. NUMBER OF PAGES	19a. NAME OF RESPONSIBLE PERSON
a. REPORT	b. ABSTRACT	c. THIS PAGE			KNOPP, JEREMY
Unclassified	Unclassified	Unclassified	SAR		19b. TELEPHONE NUMBER *(Include area code)* 315-227-7006

Standard Form 298 (Rev. 8/98)
Prescribed by ANSI Std. Z39.18

Final Report for AOARD Grant FA2386-16-1-4120

"**Development of γ' precipitation-strengthened W-free Co-base superalloys for gas turbine applications**"

2019.07.11

Name of Principal Investigators (PI and Co-PIs): Pyuck-Pa Choi

- e-mail address : p.choi@kaist.ac.kr
- Institution : Korea Advanced Institute of Science and Technology
- Mailing Address : W1, KAIST, 291 Daehak-ro, Yuseong-gu, Daejeon 34141, Korea
- Phone : +82-42-350-3321
- Fax : +82-42-350-3310

Period of Performance: 07/01/2016-06/30/2019

Abstract

In this project we have explored new Co-Ti-based alloys forming a two-phase γ/γ' microstructure with cuboidal γ' precipitates of 60 ~ 70% volume fraction and + 0.5 ~ 1.0% lattice misfit. Such a microstructure is well-known from modern Ni-based superalloys, used in aerospace gas turbine applications, and is reported to be highly beneficial for high-temperature strength and creep resistance. However, the simple binary Co-Ti system cannot meet the above-mentioned criteria for the γ/γ' microstructure, and hence, the aim of the second stage of this project is to identify multicomponent Co-Ti-based alloys forming the desired γ/γ' microstructures. The binary Co-Ti reference system, ternary Co-Ti-X (X=Cr, V, Mo, W) and quaternary Co-Ti-X-Y (X=Mo, W, Y=Cr, Al) alloys were investigated with respect to their microstructure and their high-temperature strength. Aged alloys were characterized using scanning electron microscopy (SEM), X-ray diffraction (XRD), and atom probe tomography (APT). APT analyses were performed to elucidate the elemental partitioning and site-occupation behavior of specific alloying elements and understand the changes in γ' volume fraction and morphology upon alloying. The phase transition temperatures at elevated temperatures were measured by differential scanning calorimetry (DSC). By combining all the above-mentioned characterization techniques, we could

elucidate the role of the alloying elements on lattice misfit and γ' thermal stability. Also, mechanical properties of Co-Ti-based alloys at various temperatures were studied based on uniaxial compression test. Their deformation mechanism with varying temperatures and alloying elements were elucidated utilizing transmission electron microscopy (TEM) and electron channeling contrast imaging (ECCI).

Introduction

Superalloys strengthened by γ' precipitates show outstanding high-temperature properties such as creep, oxidation, and hot corrosion resistance and are therefore the key materials in jet propulsion gas turbines. Recently, Co-based superalloys have attracted a great deal of attention for high-temperature applications. The interest in these new emerging alloys was triggered by the discovery of a γ/γ' microstructure in the ternary Co-Al-W system, which is very similar to that of high-performance Ni-based superallloys. However, the main drawbacks of Co-Al-W-based superalloys are a limited γ' phase stability and relatively low γ' solvus temperatures (usually below ~ 1300 K). Moreover, they show a high density (about 10% higher than commercial Ni-alloys) due to the high amount of W (~ 10 at.%), which limits creep rupture life.

The aim of this project is to develop new γ'-strengthened alloys based on the Co-Ti system instead of Co-Al-W.

By choosing Co-Ti as the base system, we expect to obtain alloys with enhanced thermal stability, as Co-Ti is the only known binary Co system, which forms γ' as a thermodynamically stable equilibrium phase. Furthermore, by designing W-free or W-reduced alloys, we aim to reduce the alloy density and hence to enhance the high-temperature specific strength and creep resistance. However, there are also several challenges associated with Co-Ti alloys which must be overcome. First, the lattice misfit between γ' (Co_3Ti) precipitates and γ matrix is large. Secondly, the γ' volume fraction in binary Co-Ti alloys is low due to the large solubility of Ti in Co. Thirdly, the γ' solvus temperature is low (below ~1300 K), limiting the thermal stability of the microstructure. Keeping in mind these characteristics of binary Co-Ti alloys, more advanced alloys with optimized properties must be developed.

In this project we systematically investigated the effects of the alloying elements Cr, V, Mo, and W on the microstructure, lattice mismatch, thermal stability, and mechanical properties of ternary Co-Ti-X (X=Cr, V, Mo, W) and quaternary Co-Ti-X-Y alloys (X: Mo, W, Y: Cr, Al).

Experimental

Binary Co-Ti, ternary Co-Ti-X (X=Cr, V, Mo, W) and quaternary Co-Ti-X-Y (X=Mo, W, Y=Cr, Al) alloys were prepared by vacuum arc re-melting, where the samples were re-melted several times to reduce segregation and chemical inhomogeneity. As-cast alloys were homogenized at (or around) 1150°C for 24 h (or 120 h) to minimize micro-segregation, followed by an aging treatment at 800°C (900°C for Co-Ti-W) for 24 h to form a γ/γ' microstructure. For all the heat treatments, the alloys were encapsulated in quartz tubes back-filled with Ar gas. For microstructural characterization, scanning electron microscopy (SEM) was performed using a Zeiss Merlin and Hitachi SU820 instrument both in the secondary electron (SE) and backscatter electron (BSE) imaging mode. For obtaining a topological contrast in the SE mode, the samples were etched with a solution of 20 ml of HCl and 1 ml of H_2O_2.

To measure the γ/γ' lattice misfit, X-ray diffraction (XRD) was performed using a RIGAKU Smartlab instrument, where the XRD patterns were evaluated with the software PDXL (RIGAKU). Detailed scans of (111) Bragg reflections were performed in the angular range from 42 to 45° at a step size of 0.01° or 0.02° and scan rates 0.1°/min to 1°/min. Two distinct Pseudo-Voigt functions were used for fitting the (111) reflections and for determining the lattice parameters of the γ and γ' phases. The characteristic phase transition temperatures of aged alloys were obtained from differential scanning calorimetry (DSC) at a heating rate of 10K/min under constant argon gas flow, using a NETZSCH DSC 404C instrument.

Phase compositions, elemental partitioning and in specific cases the sub-lattice occupancy within the γ' phase were measured with APT. To accurately resolve the [001] lattice planes for site occupancy investigation, grains with [001] orientation were identified using electron backscatter diffraction (EBSD). Wedge-shaped bars were cut and lifted out from those grains using a focused ion beam (FIB) instrument (Helios NanoLab 600i). The bars were attached to commercial flat-top Si microtips and subsequently FIB milled to needle-shaped APT specimens. The specimens were cleaned by a final step at 5 kV acceleration voltage and a current of 41 pA to remove the regions severely damaged by Ga implantation. APT measurements were performed at the Max-Planck-Institut fuer Eisenforschung in

Duesseldorf/Germany with a Cameca LEAP 5000XS system in pulsed laser mode (laser wavelength of 355 nm) at a specimen base temperature of 40 K. A laser pulse frequency of 200 kHz and a pulse energy of 40 pJ were applied. For Co-Ti-W-based alloys, a LEAP 4000X HR system, installed at the Pohang Institute of Science and Technology (POSTECH), was used. Measurements were performed in pulsed laser mode (laser wavelength of 355 nm) at a temperature of 70 K, a laser pulse frequency of 200 kHz, and a pulse energy of 60 pJ. Data analyses were performed with the software IVAS™ 3.6.14. Uniaxial compression tests were carried out at room temperature, 600, 700, 800, and 900°C at a strain rate of $10^{-4}s^{-1}$ using a high temperature universal testing machine (UTM) (MTS 810). For the microstructural investigation of deformed samples, compression experiments were interrupted at a strain of 2% (Co-Ti alloys tested at room temperature and 700°C) and 6% (Co-Ti, Co-Ti-Mo and Co-Ti-Mo alloys tested at room temperature, 700 and 800°C) and the samples were water-quenched. A Zeiss Merlin and Cs-corrected STEM (Titan, FEI) operated at 300 kV were used for ECCI and STEM analysis, respectively. TEM samples were prepared using the FIB lift-out method (Helios 600i, FEI).

Results and Discussion

1. Microstructures of aged binary Co-Ti / ternary Co-Ti-X (X=Mo, W, V, Cr) alloys

1-1. Microstructures of aged binary Co-Ti / ternary Co-Ti-X (X=Mo, V, Cr) alloys

Figure 1 (a) shows a grain boundary region of an aged Co-12Ti at.% sample (denoted as Co-12Ti). No additional phase other phases than γ and γ' could be observed even at the grain boundary. Thus, the aged Co-12Ti alloy exhibited a two-phase γ/γ' microstructure, where plate-shaped γ' precipitates (black regions in Figure 1 (b)) rather than cubic were formed in the γ matrix (white regions in Figure 1 (b)). The plate-shaped γ' morphology suggests that the γ/γ' interfaces could be semi-coherent.

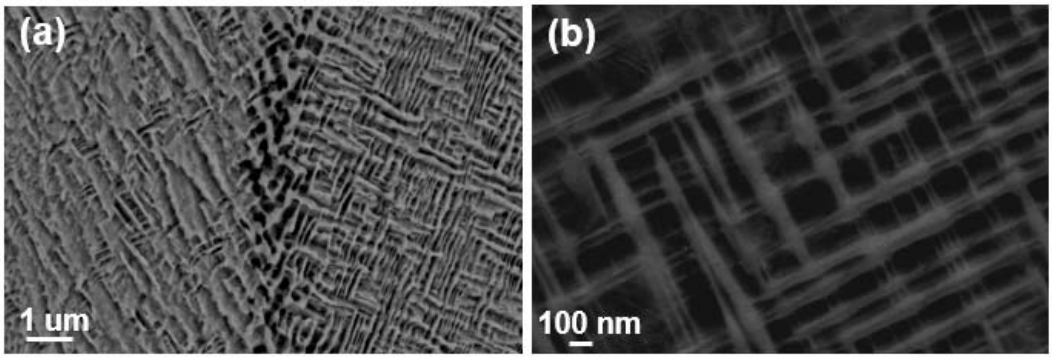

Figure 1. SEM images of Co-12Ti aged at 800˚C for 24 h: (a) low-magnification BSE image and (b) high-magnification BSE image.

Mo is a slowly diffusing refractory element and is hence expected to enhance the creep resistance of the Co-12Ti base alloy. In this study we added 4 at.% Mo to the alloy at the expense of Co (denoted as Co-12Ti-4Mo). The SEM images in Figure 2 (a) and (b) show a two-phase γ/γ' microstructure. Figure 2 (b) shows more cuboidal γ' precipitates and an increased γ' volume fraction for the ternary Co-12Ti-4Mo alloy as compared to the base Co-12Ti alloy. The transition from plate-shaped to cuboidal precipitate morphology suggests that lattice misfit value has decreased upon alloying with Mo.

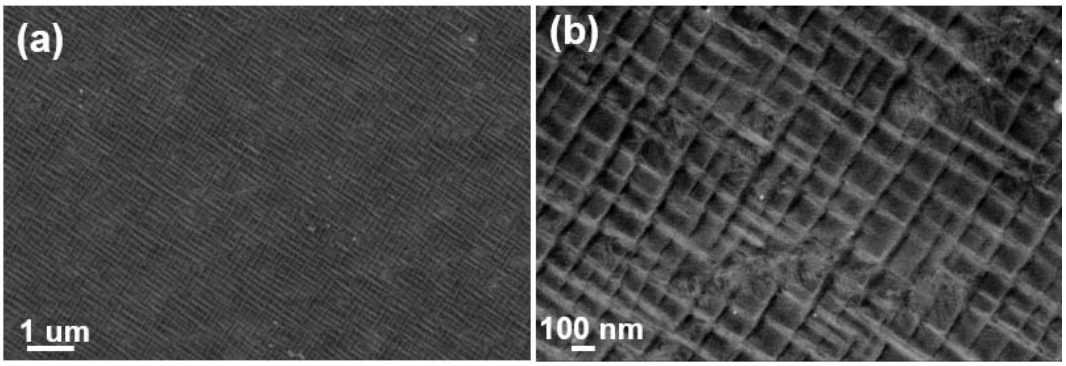

Figure 2. SEM images of Co-12Ti-4Mo aged at 800˚C for 24 h: (a) low-magnification BSE image and (b) high-magnification SE image.,

Thermodynamic calculations predict a large solubility of V in γ' (Co_3Ti). Hence, V could significantly increase the γ' volume fraction. We performed homogenization at 1130°C for 24 h and aging at 900°C for 24 h and obtained the desired two-phase γ/γ' microstructure. Fig. 3 (a) and (b) show SEM images of an as-homogenized and aged Co-12 at.% Ti-4 at.% V sample (denoted as Co-12Ti-4V), respectively.

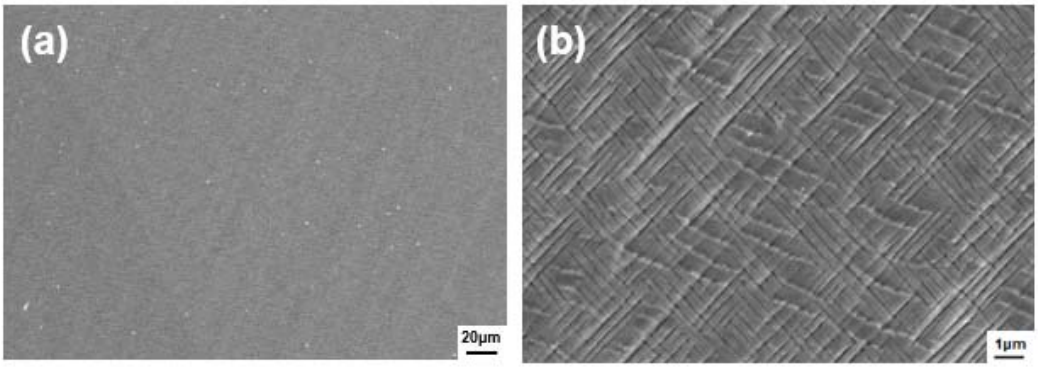

Figure 3. SE images of Co-12Ti-4V (a) homogenized at 1130°C for 24 h and (b) aged at 900°C for 24 h.

Cr is expected to improve the oxidation resistance of Co-12Ti alloys by inducing the formation of Cr_2O_3 passivation layers. Co-12 at.% Ti-4 at.% Cr (denoted as Co-12Ti-4Cr) alloys were therefore investigated. The SEM images in Figure 4 (a) and (b) confirmed a two-phase γ/γ' microstructure with cuboidal γ' precipitates. Surprisingly, the γ' volume fraction was strongly increased as compared to the Co-12Ti base alloy, though Cr is known to be a γ former. This phenomenon is related to the sub-lattice occupancy of Cr in γ', as discussed below.

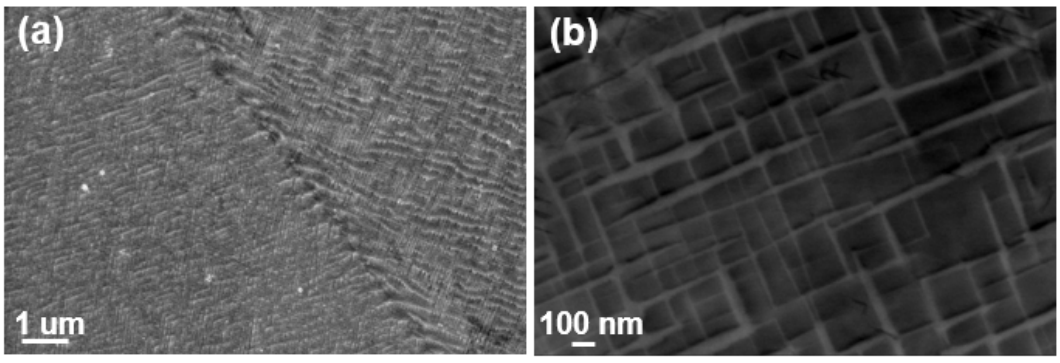

Figure 4. SEM images of Co-12Ti-4Cr aged at 800˚C for 24 h: (a) low-magnification SE age at grain boundary region and (b) high-magnification BSE image.

1-2. Microstructures of aged ternary Co-Ti-W alloys

A moderate amount of 3 at.% W is expected to enhance creep resistance and high-temperature γ' thermal stability, while maintaining the alloy density at a reasonably low level as compared to the well-known Co-Al-W, for which up to 10 at.% of W are added. Figure 5 (a) and (b) show the microstructure of the Co-15 at.% Ti-3 at.% W alloys (denoted as Co-15Ti-3W) with cuboidal γ' precipitates embedded in the γ matrix. Adding 3 at.% W to the Co-Ti base alloy led to an increase in γ' volume fraction and to a transition from plate-shaped to cuboidal γ' morphology, similar to the effect of alloying with Mo.

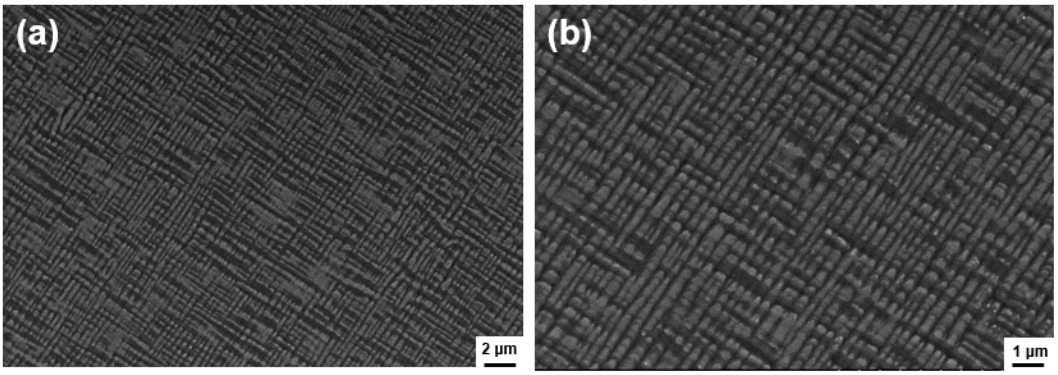

Figure 5. SEM images of Co-15Ti-3W aged at 900°C for 24 h: (a) low-magnification SE image and (b) high-magnification SE image.,

2. Microstructures of aged quaternary Co-Ti-X-Y (X=Mo, W, Y=Cr, Al) alloys

2-1. Microstructures of aged quaternary Co-Ti-X-Y (X=Mo, Y=Cr, Al) alloys

For improving the oxidation and corrosion resistance and reducing the alloy density, 2 and 4 at.% of Cr and Al were added to Co-12Ti-4Mo (denoted as Co-12Ti-4Mo-2Cr, Co-12Ti-4Mo-4Cr, Co-12Ti-4Mo-2Al and Co-12Ti-4Mo-4Al) as quaternary elements.

Figure 6 shows SEM images of aged Co-12Ti-4Mo-based quaternary alloy samples. They all exhibited γ/γ' microstructures where cuboidal γ' precipitates of high volume fractions were embedded in the γ matrix. γ' precipitates in Co-12Ti-4Mo-2Cr and Co-12Ti-4Mo-4Cr exhibited rather round corners than those in Co-12Ti-4Mo-2Al and -4Al, which is thought to be due to a γ/γ' lattice misfit decrease with the addition of Cr. Changes in γ/γ' lattice misfit with alloying element additions will be discussed below.

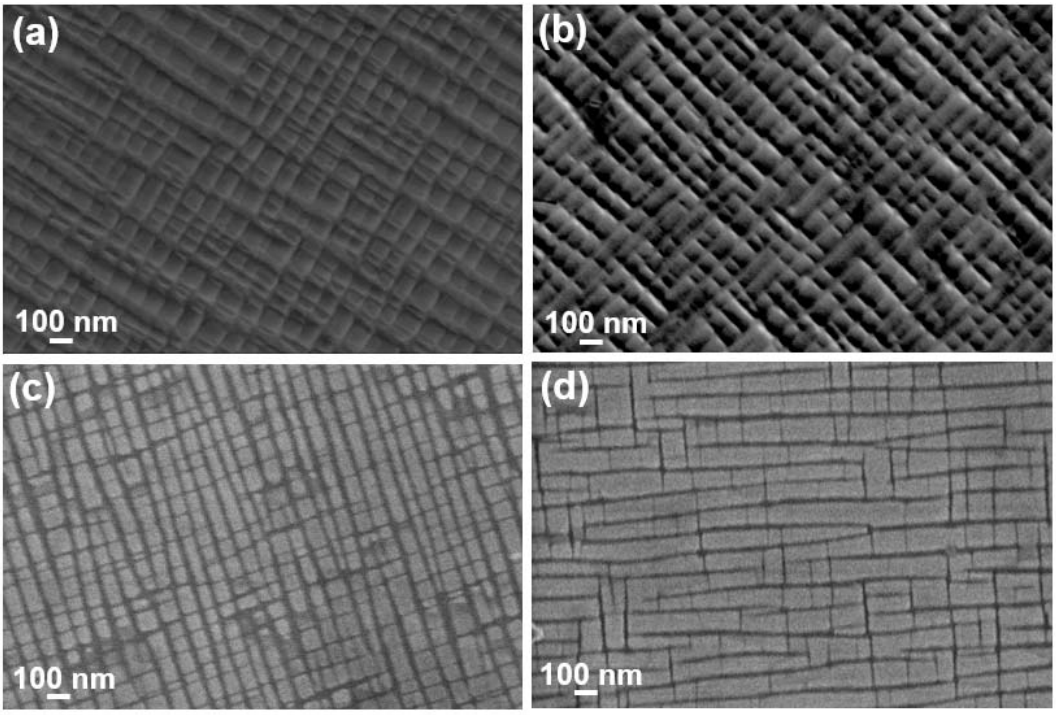

Figure 6. SE images of aged (a) Co-12Ti-4Mo-2Cr, (b) Co-12Ti-4Mo-4Cr, (c) Co-12Ti-4Mo-2Al and Co-12Ti-4Mo-4Al at 800°C for 24 h.

2-2. Microstructures of aged quaternary Co-Ti-X-Y (X=W, Y=Cr, Al) alloys

For improving the oxidation and hot corrosion resistance and reducing the alloy density, from 2 to 6 at.% of Cr and Al were added to Co-Ti-W (denoted as Co-13Ti-3W-2Cr, Co-13Ti-5W-4Cr, Co-13Ti-3W-3Al and Co-13Ti-3W-6Al) as quaternary elements. Figure 7 shows the microstructure of aged Co-Ti-W-Cr or Co-Ti-W-Al alloys. A two-phase γ/γ' microstructure could be observed for all alloys, and the addition of both Cr and Al led to significant increases in γ' volume fraction as compared to the reference Co-12Ti and Co-15Ti-3W alloys. The cuboidal γ' morphology of the ternary Co-15Ti-3W alloy was essentially preserved for the quaternary alloys.

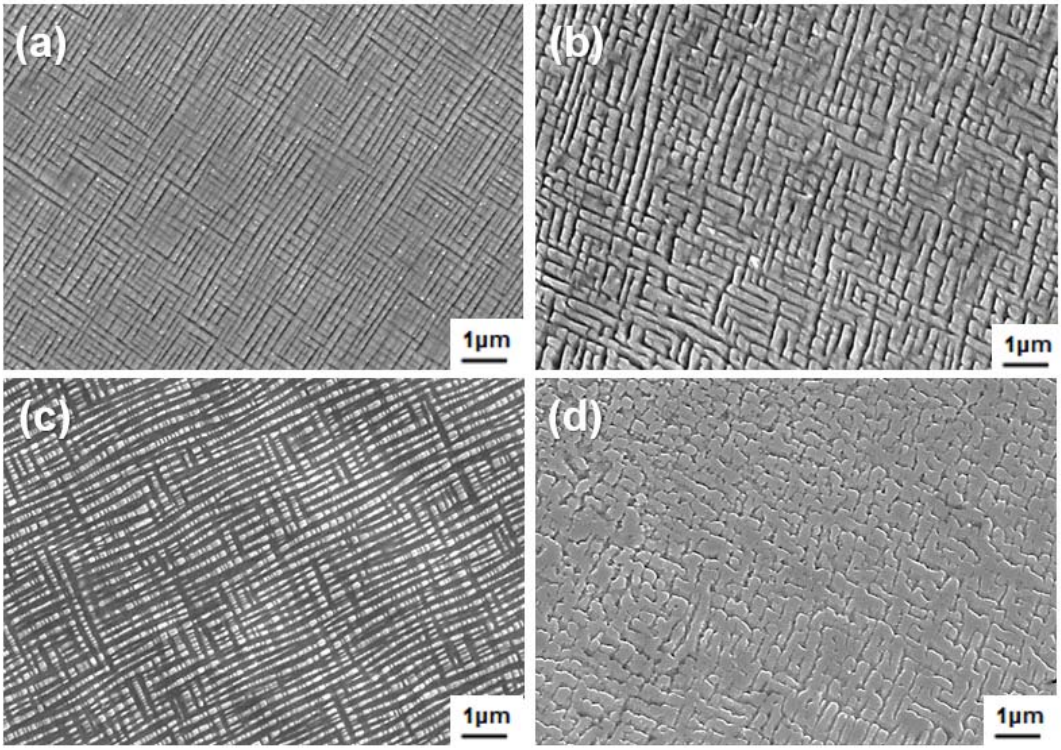

Figure 7. SE images of aged (a) Co-13Ti-3W-2Cr, (b) Co-13Ti-5W-4Cr, (c) Co-13Ti-3W-3Al and Co-13Ti-3W-6Al at 900°C for 24 h.

3. APT results of Co-Ti-based alloys (Phase compositions, γ' fractions and site-occupancy)

3-1. Binary / ternary Co-Ti-X (X=Mo, W, V, Cr) alloys

To determine phase compositions, γ' volume fractions and the site occupancy of elements in the γ' phase, APT analyses of the aged alloys were performed. Figure 8 (a) shows 3D atom map of an aged Co-12Ti sample analyzed along the [001] direction. Figure 8 (b) shows a proximity histogram across a γ/γ' interface. The proximity histogram reveals that Co partitions to the γ phase and Ti partitions to the γ' phase. The γ and γ phase compositions, elemental partitioning coefficients ($K_i = C_i^{\gamma'}/C_i^{\gamma}$), and γ' volume fractions of the binary Co-12Ti alloy and all studied ternary alloys are listed in Table 1. Individual γ and γ' phase regions were selected from the APT datasets to determine the phase compositions from evaluation of mass spectra. The γ' phase in Co-12Ti alloys exhibits a composition of nearly 80 at.% of Co and 20 at.% of Ti, which suggests the existence of point defects, i. e. Co_{Ti} anti-site defects or Ti vacancies, in the Co_3Ti phase.

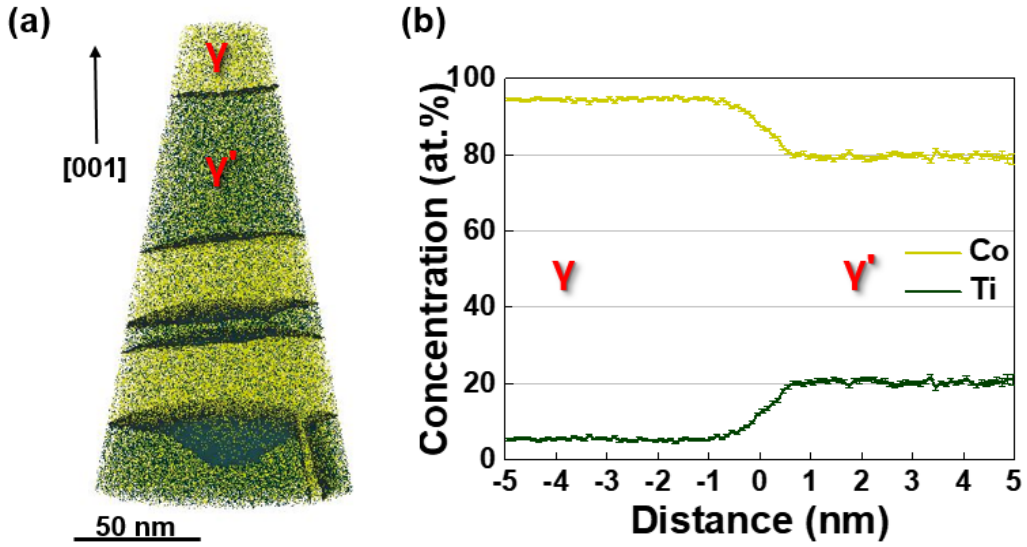

Figure 8. (a) APT reconstruction of the tip aligned along the [001] direction for Co-12Ti binary alloys. γ/γ′ interfaces are highlighted by 12.65 at.% Ti isoconcentration surfaces. (b) Proximity histogram across a γ/γ′ interface (12.65 at.% Ti isoconcentration surface is the chosen reference γ/γ′ interface).

Table 1. γ/γ′ phase compositions, partitioning coefficients, and γ′ volume fractions for aged Co-Ti and Co-Ti-based ternary alloys.

System		Co-12Ti	Co-12Ti-4Mo	Co-12Ti-4Cr	Co-12Ti-4V	Co-15Ti-3W
γ′ concentration (at.%)	Co	79.8	79.1	79.6	79.4	78.4
	Ti	20.2	16.4	17.1	15.7	17.8
	Ternary	-	4.5	3.4	4.9	3.8
γ concentration (at.%)	Co	93.6	93.8	88.9	92.3	89.9
	Ti	6.4	4.9	6.6	5.3	8.7
	Ternary	-	1.2	4.5	2.4	1.4
Partitioning Coefficients	Co	0.9	0.8	0.9	0.9	0.9
	Ti	3.2	3.3	2.6	3.0	2.0
	Ternary	-	3.7	0.8	2.1	2.7
γ′ vol. fraction (%)		40.7	65.3	51.8	64.2	66.6

With the phase composition values acquired from APT analyses, the γ' volume fractions were calculated using the lever rule (mass balance equation). If the difference in molar volume of γ and γ' is neglected (which is reasonable because of the similarity of the crystal structures and lattice parameters) the mass balance equation reads:

$$C_X^{\gamma}\left(1-f_{\gamma'}\right)+C_X^{\gamma'}\cdot f_{\gamma'}=C_X^{\text{no min al}}$$

$f_{\gamma'}$ is the gamma prime volume fraction, $C_x^{\gamma'}$ and C_x^{γ} are the concentrations of element X in the corresponding phases, and C_x^{nominal} is the nominal concentration of X in the alloy. This equation can be rewritten as:

$$f_{\gamma'}=\frac{\left(C_X^{\text{no min al}}-C_X^{\gamma}\right)}{\left(C_X^{\gamma'}-C_X^{\gamma}\right)}$$

The concentration values for each alloying element are plotted on a graph to perform a linear regression analysis, as shown in Figure 9. The γ' volume fraction determined from the lever rule is about 65.3% for the Co-12Ti-4Mo ternary alloy (see Table 1), which is around the optimum volume γ' fraction range of commercial Ni-based superalloys (60~70%).

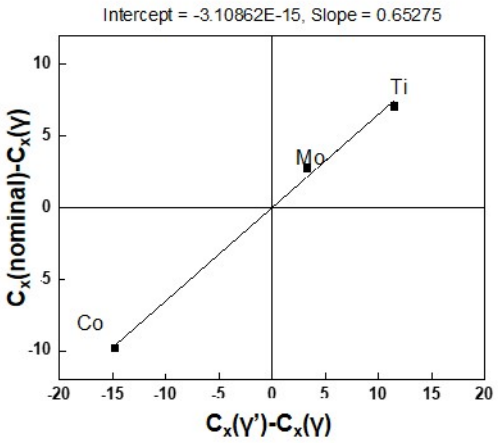

Figure 9. Lever rule plot used for calculating the γ' volume fraction of aged Co-12Ti-4Mo.

Figure 10 (a) presents [001] lattice planes resolved in both γ and γ′ phases (yellow green: Co atom, dark green: Ti atom). The γ/γ′ interfaces are highlighted by Ti iso-concentration surfaces encompassing regions of ≥ 12.65 at.% Ti. Ti atoms are observed to occupy every second plane in γ′, as marked by red arrows, which is consistent with the occupation sites of Ti in a $L1_2$-ordered structure. Element-specific spatial distribution maps (SDMs) were calculated along the z-direction. SDMs were acquired in both the γ and γ′ phase along the [001] direction, as shown in Figure 10 (b). Within γ, the SDMs of Co and Ti exhibit peaks at an average interspacing of approximately 0.18 nm, corresponding to the {002} plane spacing. In contrast, the SDM of Co in γ′ reveals alternating high and low peaks every 0.18 nm, whereas for Ti, peaks appear at an average distance of 0.36 nm. These findings give clear evidence for $L1_2$-type ordering of Co and Ti.

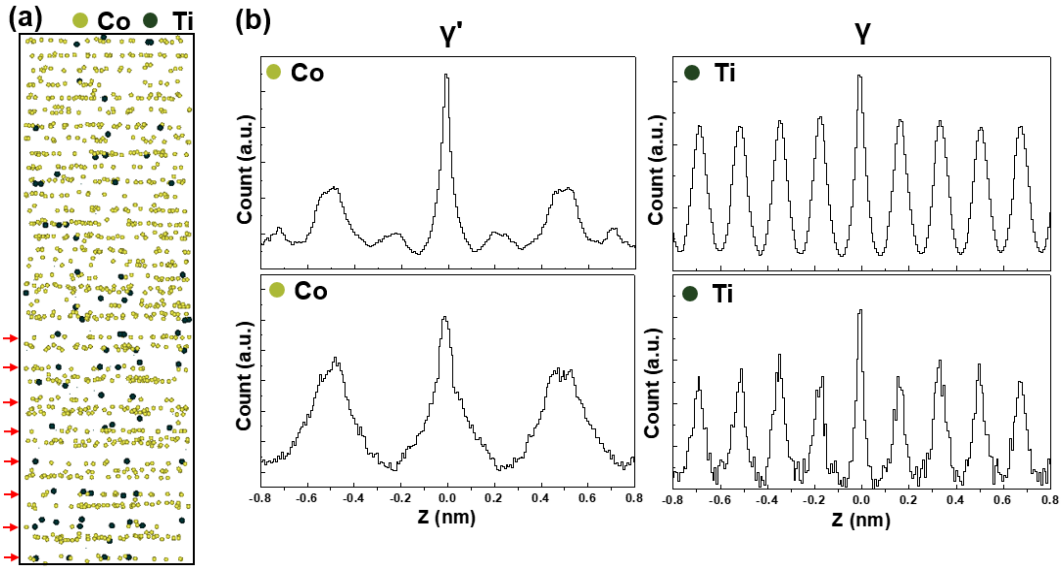

Figure 10. (a) Resolved [001] lattice planes in γ and γ′ phases in an aged Co-12Ti sample. (b) Spatial distribution maps (SDMs) of Co and Ti in γ and γ′ phases along the [001] direction.

Figure 11 (a) and (c) and 12 (a) and (c) show 3D atom maps of Co-Ti-X (X=Cr, V, Mo, W) ternary alloys. Figure 11 (b) and (d) and Figure 12 (b) and (d) show proximity histograms across γ/γ′ interfaces (left : γ phase, right : γ’ phase). In all proximity histograms, elemental partitioning between γ and γ′ could be clearly revealed. Ti, Mo, V and W atoms partitioned to the γ’ phase, whereas Co and Cr partitioned to the γ phase. Mo, V and W refractory atoms partitioned to γ’ and thereby increased the γ’ volume fraction and thermal stability.

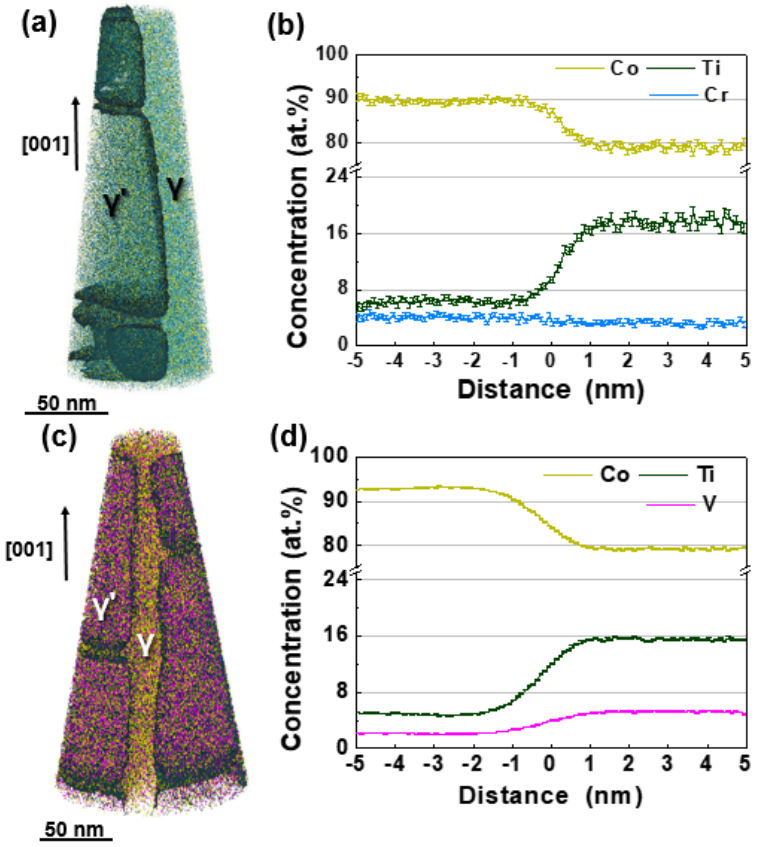

Figure 11. APT reconstructions of the tips aligned along the [001] direction for (a) Co-12Ti-4Cr (12.65 at.% Ti iso-concentration surface) and (c) Co-12Ti-4V (11.23 at.% Ti iso-concentration surface). Proximity histogram across γ/γ′ interfaces for (b) Co-12Ti-4Cr and (d) Co-12Ti-4V.

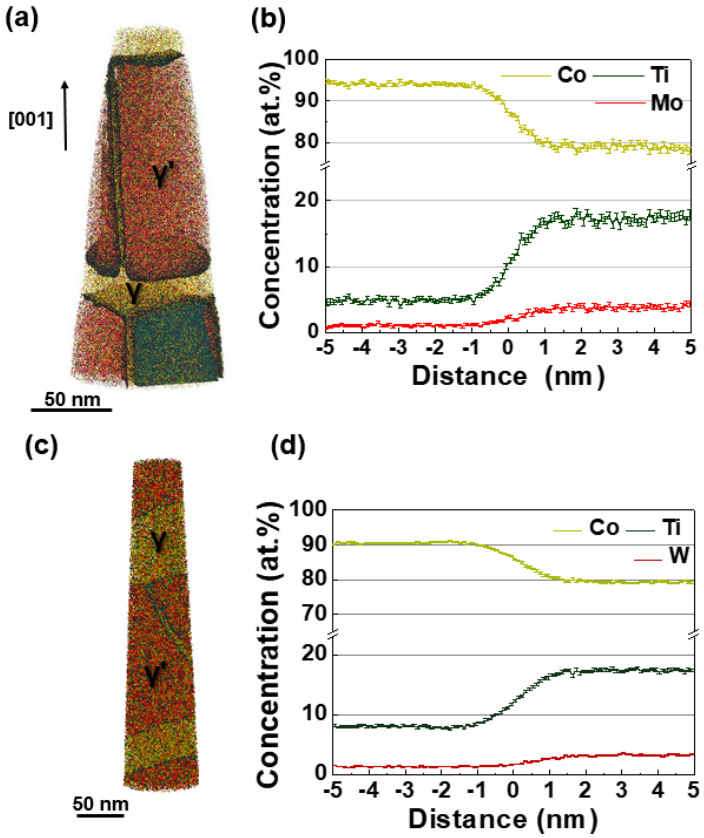

Figure 12. APT reconstructions of the tips aligned along the [001] direction for (a) Co-12Ti-4Mo (10.36 at.% Ti iso-concentration surface) and (c) Co-15Ti-3W (13.32 at.% Ti iso-concentration surface). Proximity histograms across γ/γ′ interfaces for (b) Co-12Ti-4Mo and (d) Co-15Ti-3W.

Figure 13 (a) to (c) show SDMs calculated along the [001] direction in γ′ for Co-12Ti-4Mo, Co-12Ti-4V and Co-12Ti-4Cr. Mo, V, and Cr show periodic peaks with an average interspacing of about 0.36 nm, identical to Ti (Figure 10 (b)). We could not acquire accurate SDMs for the Co-15Ti-3W system since a large difference in evaporation field of W and other atoms degraded the spatial resolution of the APT analyses.

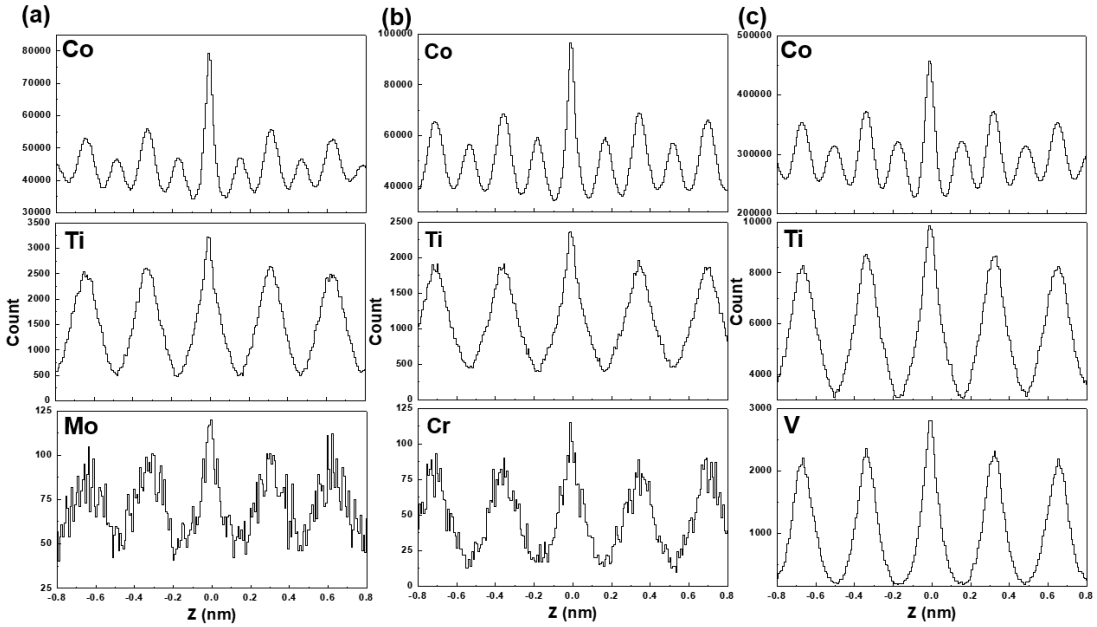

Figure 13. Spatial distribution maps (SDMs) of Co, Ti and ternary alloying elements in γ′ phases along the [001] direction for (a) Co-12Ti-4Mo, (b) Co-12Ti-4Cr, and (c) Co-12Ti-4V alloys.

As can be seen in Table 1, the sum of Ti and ternary elements concentrations in γ' phase is around 21 at.%, whereas the Co concentration is around 79 at.%. SDMs (Figure 13) and concentration values (Table 1) indicate that Mo, Cr, and V share the same sub-lattice with Ti atoms in γ' precipitates. Mo, W, and V were found to act as γ' stabilizers as they strongly partitioned to γ'.

Due to a high evaporation field of W (52 V/nm) compared to Co (37 V/nm) and Ti (26 V/nm), the measured compositions of W at γ and γ′ phases were less than 4 at.%, as shown in Table 1. W atoms were preferentially retained on the APT specimen during pulsed laser APT analyses and, resulting in a lower apparent W concentration than expected.

With the addition of ternary elements, the γ' volume fraction increased from 40.7% for Co-12Ti to about 65.3%, 51.8%, 64.2% and 66.6% for Co-12Ti-4Mo, Co-12Ti-4Cr, Co-12Ti-4V and Co-15Ti-3W respectively (see Table 1). For the Co-12Ti-4Mo and Co-12Ti-4V system, the Ti concentration in γ' significantly dropped from 20.2 at. % to 16.4 at.% and 15.7 at.%, respectively (compare with Table 1). Furthermore, the solubility of Ti in

γ appeared to be reduced by the addition of Mo or V to the binary alloy, as the Ti concentration was 4.9 at.% Ti in Co-12Ti-4Mo and 5.31 at.% Ti in Co-12Ti-4V, as compared to 6.4 at.% Ti in aged Co-12Ti. As Ti has a strong tendency to partition to γ', excess Ti resulting from partial substitution of Ti by Mo or V in γ' contributed to the formation of additional γ'. Strong partitioning of alloying elements to γ' and its tendency to occupy the Ti sub-lattice within γ' as well as a reduced Ti solubility in γ resulted in increases in the γ' volume fraction upon alloying with Mo or V.

With the addition of Cr, the Ti concentration in γ' decreased to 17.1 at.%. Although Cr preferentially partitioned to γ, Cr in γ' mostly substituted Ti, thus leading to an increase in γ' volume fraction, by virtue of the same mechanism as for Mo and V. However, the solubility of Ti in γ was little affected by Cr, which led to a modest increase in γ' volume fraction for Co-12Ti-4Cr as compared to the Co-12Ti alloy.

3-2. Quaternary Co-Ti-X-Y (X=Mo, Y=Cr, Al) alloys

Figures 14 (a), (c), and (e) show 3D atom maps of Co-12Ti-4Mo-2Cr, Co-12Ti-4Mo-4Cr, and Co-12Ti-4Mo-2Al. The proximity histograms across γ/γ′ interfaces (see figure 14 (b), (d), and (f), left : γ phase, right : γ' phase) revealed the same partitioning behavior for Mo and Cr as in ternary alloys. Phase compositions, partitioning coefficients, and γ' volume fractions calculated using the lever rule, are listed in Table 2 for the Co-12Ti-4Mo-based alloys. Table 2 reveals that Al weakly partitioned to γ with a partitioning coefficient of 0.8, as compared to Cr (partitioning coefficient of 0.7) in the Co-12Ti-4Mo-2Cr alloy.

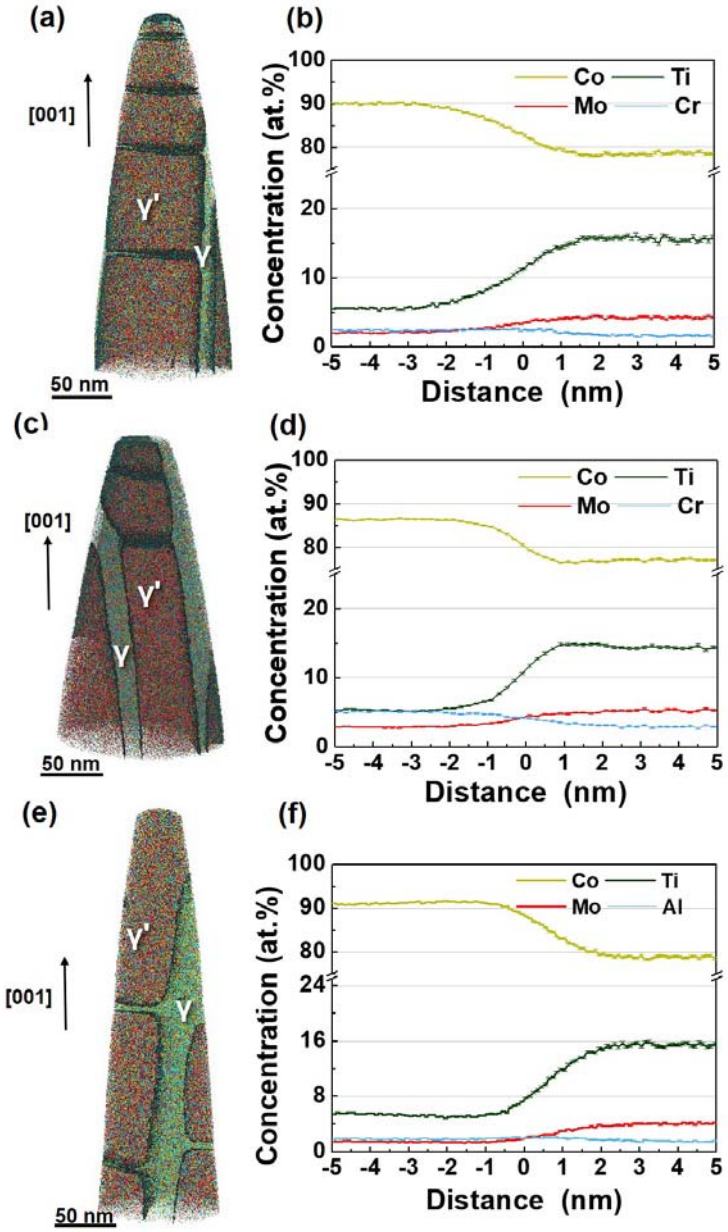

Figure 14. APT reconstructions of tips aligned along the [001] direction for (a) Co-12Ti-4Mo-2Cr (10.66 at.% Ti iso-concentration surface), (c) Co-12Ti-4Mo-4Cr (8.00 at.% Ti iso-concentration surface) and (e) Co-12Ti-4Mo-2Al (10.20 at.% Ti iso-concentration surface). Proximity histogram across γ/γ′ interfaces for (b) Co-12Ti-4Mo-2Cr, (d) Co-12Ti-4Mo-4Cr and (f) Co-12Ti-4Mo-2Al.

Table 2. γ/γ′ phase compositions, partitioning coefficients, and γ′ volume fractions for Co-12Ti-4Mo-based alloys

System		Co-12Ti-4Mo	Co-Ti-Mo-2Cr	Co-Ti-Mo-4Cr	Co-Ti-Mo-2Al
γ′ concentration (at.%)	Co	79.1	78.9	77.7	78.5
	Ti	16.4	15.1	15.2	15.8
	Mo	4.5	4.5	4.0	4.1
	Cr/Al	-	1.5	3.0	1.5
γ concentration (at.%)	Co	93.8	90.2	87.5	91.0
	Ti	4.9	5.5	5.1	5.6
	Mo	1.2	2.0	2.0	1.6
	Cr/Al	-	2.3	5.4	1.9
Partitioning Coefficients	Co	0.8	0.9	0.9	0.9
	Ti	3.3	2.7	3.0	2.8
	Mo	3.7	2.2	2.0	2.7
	Cr/Al	-	0.7	0.6	0.8
γ′ vol. fraction (%)		65.3	70.9	72.4	68.9

Figure 15 shows SDMs calculated along the [001] direction in γ' for both Co-12Ti-4Mo-2Cr and Co-12Ti-4Mo-4Cr alloys. Due to a low evaporation field of Al atoms, SDMs of Al-added alloys could not be acquired. The SDMs of Ti, Mo, and Cr in the γ' phase of the Co-12Ti-4Mo-2Cr alloy (Figure 15 (a)) show peaks with an interspacing of about 0.36 nm, which indicates that Mo and Cr occupy the Ti-sublattice in γ'. With increasing Cr concentration from 2 to 4 at.%, changes in the interspacing Mo peaks were observed (Figure 15 (b)). The peaks showed an interspacing of 0.18 nm, which correspond to the interspacing of Co peaks and Ti. This finding suggests that there is a competition between Mo and Cr for the Ti-sublattice and excessive amounts of Cr partially drive the Mo atoms into the Co sub-lattice.

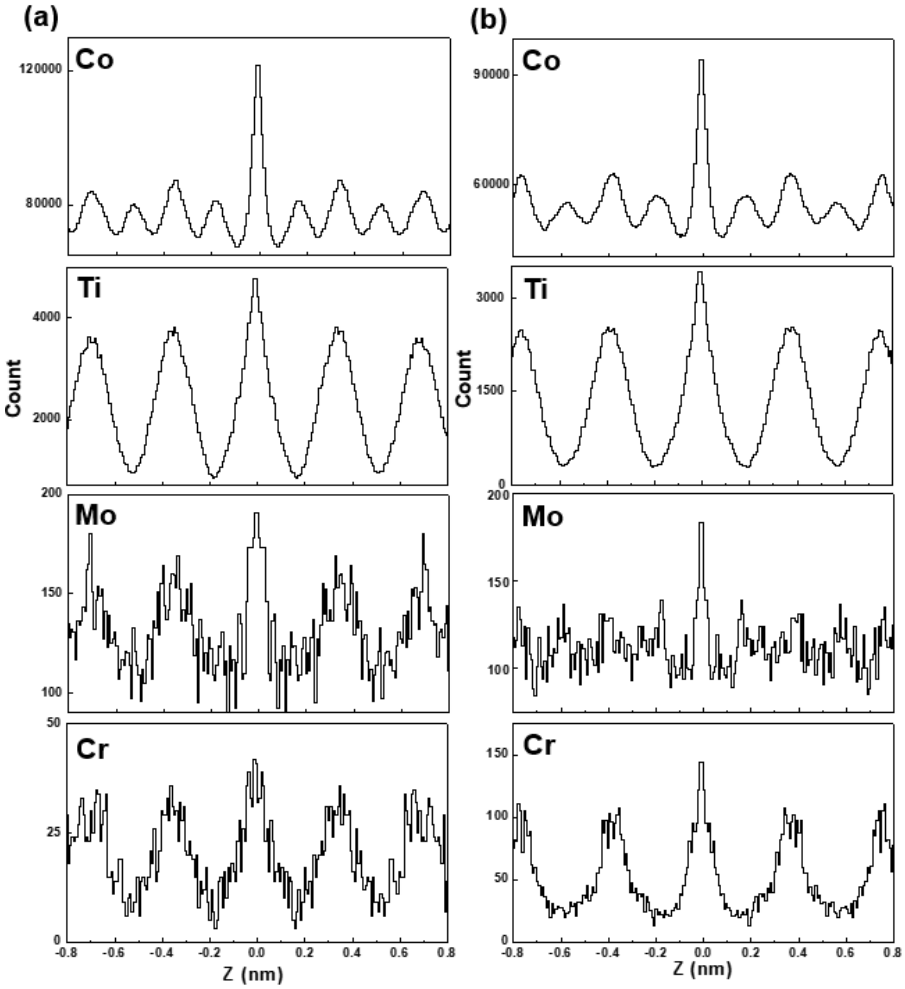

Figure 15. Spatial distribution maps (SDMs) of Co, Ti, Mo, and Cr in γ′ phases along the [001] direction for (a) Co-12Ti-4Mo-2Cr and (b) Co-12Ti-4Mo-4Cr alloys.

In Table 2, all quaternary alloys showed further increases in γ' volume fraction as compared to the ternary Co-12Ti-4Mo. The resulting γ' volume fractions were around the optimum value for high-temperature creep resistance in Ni-based superalloys. Both Mo and Cr were found to occupy the Ti-sublattice. In the Co-12Ti-4Mo-2Cr alloys, the Ti concentration in γ' decreased due to the partial substitution of Ti by Cr atoms, while Ti concentration in γ was less affected. Thus, a decrease in the partitioning coefficient of Ti from 3.3 (Co-12Ti-4Mo) to 2.7 (Co-12Ti-4Mo-2Cr) was measured. The Mo concentration in γ increased and therefore the partitioning coefficient of Mo decreased with the addition of 2 at.% Cr. With increasing amount of Cr from 2 to 4 at.%, the γ' volume fraction increased to 72.4%. Increasing the Cr content resulted in a competition between Cr and Mo for the Ti sub-lattice sites in γ', as seen

in the SDMs in Figure 15. A decrease in Cr partitioning coefficient from 0.7 (Co-12Ti-4Mo-2Cr) to 0.6 (Co-12Ti-4Mo-4Cr) also gave evidence for the competition for limited Ti sub-lattice sites in γ'. Mo atoms pushed out from the Ti sub-lattice in γ' appeared to move to the Co sub-lattice in γ' rather than being solved in the γ phase, as the Mo concentration value (~ 2 at.%) in γ remained essentially constant for Co-12Ti-4Mo-2Cr and Co-12Ti-4Mo-4Cr. While in γ', the Mo concentration decreased by about 0.5 at.%, Mo atoms partially replaced by Cr could form additional γ', thus inducing a drop in the partitioning coefficient of Mo.

Also, it should be noted that the Co content in γ' decreased by about 1.4 at.%, which may have two reasons: one is the occupation of the Co sub-lattice Mo atoms; the other is the removal of Co_{Ti} anti-site defects by Mo.

3-3. Quaternary Co-Ti-X-Y (X=W, Y=Cr, Al) alloys

Figure 16 (a), (c), (e), and (g) show 3D atom maps of Co-12Ti-4W-Cr and Co-12Ti-4W-Al alloys. The proximity histograms in Figure 16 (b), (d), (f), and (h) clearly reveal that Ti and W atoms partitioned to the γ' phase, while Co, Cr, and Al atoms partitioned to the γ phase, which is consistent with the elemental partitioning behaviors observed for the ternary systems.

The average γ/γ' composition values, elemental partitioning coefficients, and γ' volume fractions of Co-Ti-W-based alloys are listed in Table 3. As mentioned in the section about the ternary Co-15Ti-3W alloy, the evaporation field value of W is significantly higher than those of other elements (Co: 37, Ti: 26, W: 52, Cr: 29 and Al: 19 V/nm) and preferential field retention effects lead to a loss of W atoms. As a result, the apparent concentrations of W in the alloys tended to be lower than the nominal 4 at.%.

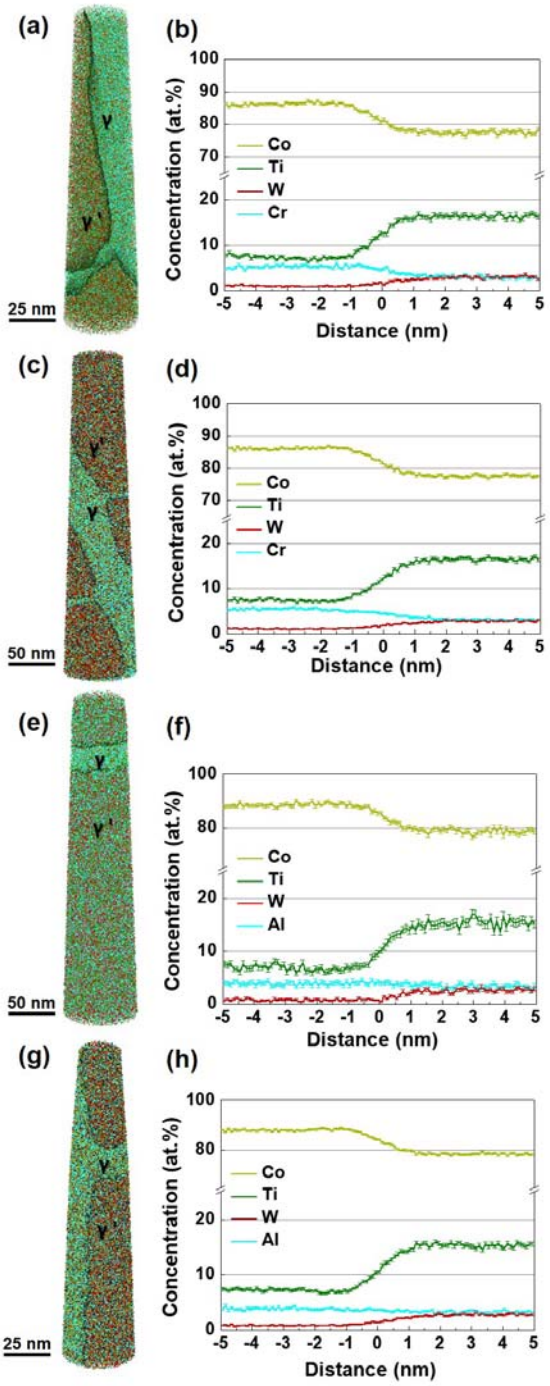

Figure 16. APT reconstructions of the tips aligned along the [001] direction for (a) Co-13Ti-3W-2Cr (11.90 at.% Ti iso-concentration surface), (c) Co-13Ti-5W-4Cr (11.82 at.% Ti iso-concentration surface), (e) Co-13Ti-3W-3Al (10.15 at.% Ti iso-concentration surface) and (g) Co-13Ti-3W-6Al (10.76 at.% Ti iso-concentration surface). Proximity histogram across γ/γ′ interfaces for (b) Co-13Ti-3W-2Cr, (d) Co-13Ti-5W-4Cr, (f) Co-13Ti-3W-3Al, and (h) Co-13Ti-3W-6Al.

Using the lever rule the γ' volume fractions were calculated (see Table 3). With the addition of Ti and W the γ' volume fraction increased from 40.7 % for the Co-12Ti binary alloy to about 66.6% for Co-15Ti-3W. However, adding about 2 at.% Cr at the expense of Ti (Co-13Ti-3W-2Cr) led to a reduction in γ' volume fraction, as Cr and Ti partitioned to γ and γ', respectively. The Co-13Ti-5W-4Cr alloy shows an increase in γ' volume fraction to 76.0% as compared to the ternary alloy due to the extra amount of W, which showed strong γ' partitioning. Adding about 3 and 6 at.% of Al to the ternary alloy at the expense of Co and Ti increased the γ' volume fraction to 77.7 and 90.9%, respectively. The effect of Al on the γ' volume fraction is at first sight surprising, as it slightly partitions to γ according to the APT results. Al appears to enhance partitioning of Ti and in particular W to γ'. As both elements are strong γ' formers the Al effect on the increase in γ' volume fraction is significant.

Table 3. γ/γ' phase compositions, partitioning coefficients, and γ′ volume fractions for Co-Ti-W-based alloys

System		Co-15Ti-3W	Co-13Ti-3W-2Cr	Co-13Ti-5W-4Cr	Co-13Ti-3W-3Al	Co-13Ti-3W-6Al
γ′ concentration (at.%)	Co	78.4	77.4	77.4	78.7	78.6
	Ti	17.8	16.6	16.6	15.3	15.1
	W	3.8	3.0	2.9	2.6	2.9
	Quaternary	-	3.0	3.1	3.4	3.4
γ concentration (at.%)	Co	89.9	86.1	85.9	88.3	88.2
	Ti	8.7	7.4	7.7	7.1	7.0
	W	1.4	1.1	1.0	0.8	0.9
	Quaternary	-	5.3	5.4	3.8	3.9
Partitioning Coefficients	Co	0.9	0.9	0.9	0.9	0.9
	Ti	2.0	2.2	2.2	2.1	2.1
	W	2.7	2.6	2.9	3.4	3.4
	Quaternary	-	0.6	0.6	0.9	0.9
γ′ vol. fraction		66.6	57.9	76.0	77.7	90.9

4. Lattice misfit measurements

The γ/γ’ lattice misfit controls the γ’ morphology and high-temperature strength of γ’–strength superalloys and is defined as follows:

$$\delta = \frac{2\left(a_{\gamma'} - a_{\gamma}\right)}{a_{\gamma'} + a_{\gamma}}$$

a_γ and $a_{\gamma'}$ are the lattice parameters of the γ and the γ' phase, respectively. The γ/γ' lattice misfit of Co-based superalloys should range from ~ + 0.5 to ~ + 1.0% to obtain a thermally stable γ/γ' microstructure and achieve coherency strain hardening. The γ/γ' lattice misfits of the aged Co-Ti-based alloys were first investigated by means of XRD. Misfit values were determined from (111) reflections. The lattice parameters of γ and γ' phases were calculated using following equation:

$$a_0 = \frac{\lambda\sqrt{h^2+k^2+l^2}}{2\sin\theta}$$

where λ is the X-ray wavelength and (hkl) is the Miller index of the lattice plane under investigation. Using two Pseudo-Voigt fit functions, the Θ value can be acquired.

Lattice parameter and misfit values from (111) XRD reflections are plotted in Figure 17. The measured lattice misfit value of Co-12Ti binary alloys was 1.17% in Figure 17 (a). This relatively large lattice misfit is the reason why the Co-Ti-based alloy is prone to precipitate coarsening even at moderate temperatures. Upon adding the ternary elements Mo, W, and Cr to the Co-Ti binary system the γ' lattice parameter slightly decreased, while the γ lattice parameter slightly increased, thus inducing a decrease in the lattice misfit. In Figure 17 (b), W had a strong effect on increasing the γ lattice parameter, while Mo and Cr decreased the γ' lattice parameter, thus resulting in reduced lattice misfits. The addition of the quaternary elements Cr or Al to Co-Ti-Mo and Co-Ti-W ternary alloys also caused a decrease in γ/γ' lattice misfits.

Co-Ti-Mo- and Co-Ti-W-based alloys showed reduced lattice misfits, which were in the range of 0.5 ~ 1.0 %. The Co-12Ti-4Mo-4Al showed a different trend from the other quaternary alloys with large increases in both lattice parameters in γ and γ'.

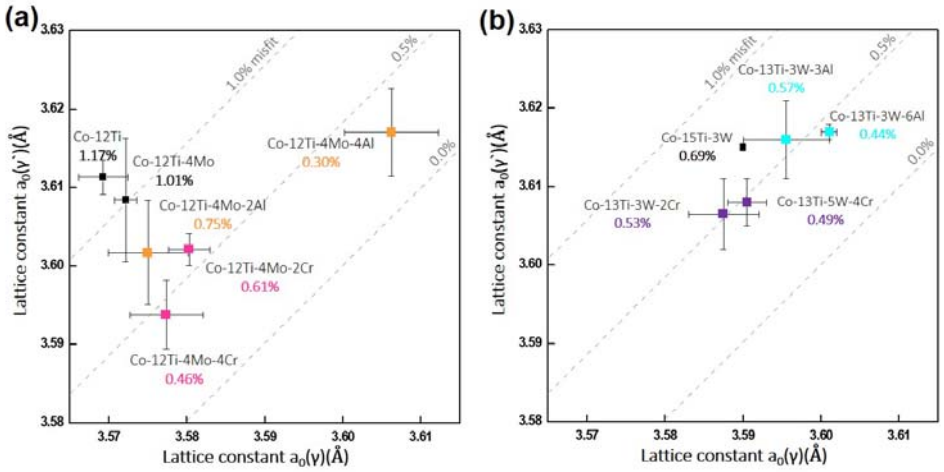

Figure 17. Lattice parameters of γ and γ' and lattice misfits of (a) Co-Ti / Co-Ti-Mo-based alloys and (b) Co-Ti-W-based alloys (The dashed lines represent 0%, 0.5%, and 1% lattice misfit values)

5. Phase transition temperatures

The γ' solvus, solidus, and liquidus temperature of the aged alloys were determined from DSC measurements and are listed in Table 4. The measured γ' solvus, solidus, and liquidus temperatures of the Co-12Ti alloy were 1005°C, 1219°C, and 1318°C, respectively. The measured γ' solvus temperatures of Co-15Ti-3W, Co-12Ti-4Mo, and Co-12Ti-4Cr were 1130°C, 1119°C and 1062°C, respectively. They were substantially higher than the γ' solvus temperature of binary Co-12Ti (1005°C) and of Co-9.2Al-9W (990°C), suggesting that W, Mo and Cr additions enhanced the thermal stability of γ'. Especially, the addition of 3 at.% of W led to a significant increase in the γ' solvus temperature. Although the W content of the Co-15Ti-3W alloy was less than half of that of Co-Al-W-based alloys (about 9~10 at.% W), the γ' solvus temperature of Co-15Ti-3W was more than 130°C higher than those of Co-Al-W alloys. These results on the ternary Co-12Ti-4Mo and Co-15Ti-3W systems were very promising, and there was room for even further improvement by tuning the alloy composition and/or adding additional elements to the Co-12Ti-4Mo and Co-15Ti-3W system.

Cr additions led to an increase in γ' solvus temperature by 20~30°C in for Co-15Ti-3W and 10~20°C for Co-12Ti-4Mo. Al additions increased γ' solvus temperatures of Co-15Ti-3W by

~ 40°C and of Co-Ti-Mo by ~ 20°C. Thus, Cr and Al also appeared to improve the thermal stability of the γ' phase. Unlike γ' solvus temperatures, alloying element additions led to decreases in solidus and liquidus temperatures.

Table 4. Phase transition temperatures for Co-Ti, Co-Ti-Mo-based, Co-Ti-W-based and Co-12Ti-4Cr alloys

	$T_{\gamma' solvus}$ (C)	$T_{solidus}$ (C)	$T_{liquidus}$ (C)
Co-12Ti	1005	1219	1318
Co-12Ti-4Mo	1119	1193	1290
Co-12Ti-4Mo-2Cr	1129	1206	1290
Co-12Ti-4Mo-4Cr	1130	1199	1283
Co-12Ti-4Mo-2Al	1139	1204	1280
Co-12Ti-4Mo-4Al	1135	1193	1269
Co-15Ti-3W	1130	1215	1318
Co-13Ti-3W-2Cr	1166	1120	1315
Co-13Ti-5W-4Cr	1152	1200	1302
Co-13Ti-3W-3Al	1172	1211	1311
Co-13Ti-3W-6Al	1174	1208	1311
Co-12Ti-4Cr	1062	1205	1321

6. Mechanical properties of Co-12Ti-4W-based alloys

Figure 18 shows the variation of the 0.2% offset compressive yield stress with temperature for the aged Co-12Ti, Co-12Ti-4Mo and Co-12Ti-4W alloy. A decrease in yield stress up to 500°C can be seen, followed by an increase in yield stress up to 700°C before the yield stress drops for higher temperatures. Such a yield stress anomaly has also been observed in other Co-based and Ni-based γ/γ' superalloys and is an important beneficial property for a high-temperature structural material.

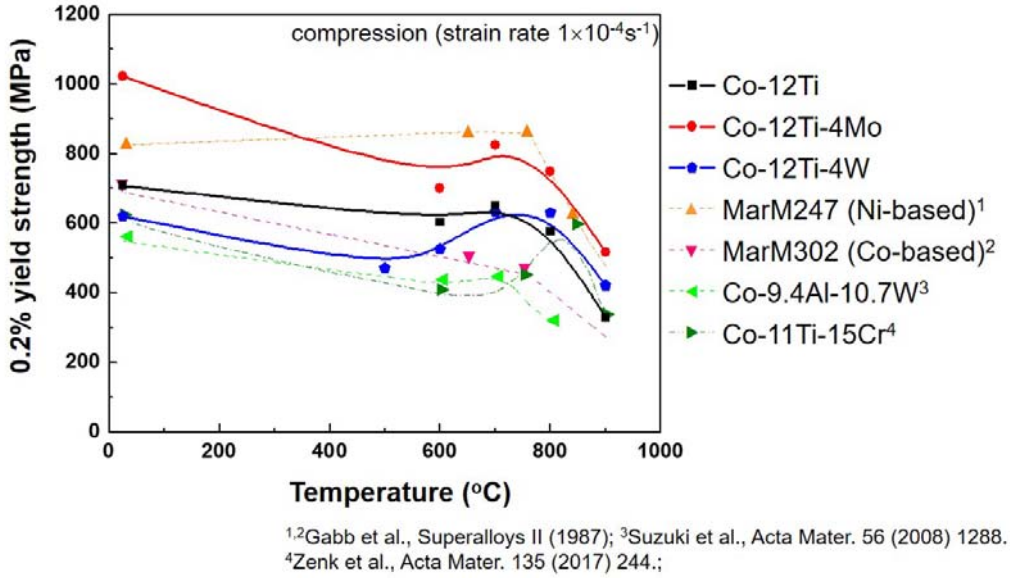

Figure 18. Variation of the 0.2% offset compressive yield stress with temperature for the aged Co-12Ti, Co-12Ti-4Mo and Co-12Ti-4W alloy in comparison with literature data.

List of Publications and Significant Collaborations that resulted from this AOARD supported project:

a) papers published in peer-reviewed journals,

1. Hye Ji Im, Surendra K. Makineni, Baptiste Gault, Frank Stein, Dierk Raabe, Pyuck-Pa Choi*, "Elemental partitioning and site-occupancy in γ/γ′forming Co-Ti-Mo and Co-Ti-Cr alloys", Scripta Materialia 154 (2018) 159-162.
2. Boryung Yoo, Hye Ji Im, Jae-Bok Seol, Pyuck-Pa Choi*, "On the microstructural evolution and partitioning behavior of $L1_2$-structured gamma`-based Co-Ti-W alloys upon Cr and Al alloying" Intermetallics 104 (2019)
3. Hyeonuk Jeong, Se-Ho Kim, Won Seok Choi, Pyuck-Pa Choi*, "Spallation resistance of oxide scales on Alloy 617 enhanced by boron addition" Corrosion Science 140 (2018)

b) conference presentations without papers,

1. Boryung Yoo, Pyuck-Pa Choi, "Microstructural changes of Co-based superalloys with alloying elements", *The 3rd East-Asia Microscopy Conference*, Novermber 07 – 10 (08), 2017, Busan, Korea.
2. Hosun Jun, Pyuick-Pa Choi, "Atomic-scale informed design of refractory multi-principle element superalloys", *The 3rd East-Asia Microscopy Conference*, Novermber 07 – 10 (08), 2017, Busan, Korea.
3. Hyeji Im, Pyuck-Pa Choi, "Elemental partitioning and site-occupancy behavior in gamma/gamma' - strengthened Co-Ti based superalloy", *2018 Spring Conference of the Korean Institute of Metals and Minerals*, April 25 – 27 (25), 2018, Jeju, Korea.
4. Boryung Yoo, Pyuck-Pa Choi, "Microstructural changes of Co-based superalloys with alloying elements", *2018 Spring Conference of the Korean Institute of Metals and Minerals*, April 25 – 27 (26), 2018, Jeju, Korea.
5. Hosun Jun, Pyuck-Pa Choi, "Atomic-scale informed design of refractory multi-principle element superalloys", *2018 Spring Conference of the Korean Institute of Metals and Minerals*, April 25 – 27 (26), 2018, Jeju, Korea.
6. Hyeji Im, Surendra K Makineni, Baptiste Gault, Dierk Raabe, Pyuck-Pa Choi, "Elemental partitioning and site occupation of Mo and Cr in Co-Ti based superalloys", *Atom Probe Tomography and Microscopy 2018*, June 10 – 15 (14), 2018, Gaithersburg, USA.

e) manuscripts submitted but not yet published, and

f) provide a list any interactions with industry or with Air Force Research Laboratory scientists or significant collaborations that resulted from this work.

Attachments: Publications a), b) and c) listed above if possible.

Scripta Materialia 154 (2018) 159–162

Contents lists available at ScienceDirect

Scripta Materialia

journal homepage: www.elsevier.com/locate/scriptamat

Regular article

Elemental partitioning and site-occupancy in γ/γ′ forming Co-Ti-Mo and Co-Ti-Cr alloys

Hye Ji Im [a], Surendra K. Makineni [b], Baptiste Gault [b], Frank Stein [b], Dierk Raabe [b], Pyuck-Pa Choi [a,*]

[a] Department of Materials Science and Engineering, Korea Advanced Institute of Science and Technology (KAIST), 291 Daehak-ro, Yuseong-gu, Daejeon 34141, Republic of Korea
[b] Max-Planck-Institut für Eisenforschung, Max-Planck-Str. 1, 40237 Düsseldorf, Germany

ARTICLE INFO

Article history:
Received 29 March 2018
Received in revised form 23 April 2018
Accepted 25 May 2018
Available online xxxx

Keywords:
Co-based superalloy
Solute partitioning
Atom probe tomography (APT)
Site occupancy

ABSTRACT

We report on the sub-nanometer scale characterization of Co-12Ti-4Mo and Co-12Ti-4Cr (at.%) model alloys. Atom probe tomography reveals that Co and Cr partition to γ, whereas Ti and Mo to γ′. Additions of Mo and Cr to the reference Co-12Ti system lead to strong increases in γ′ volume fraction by about 25% and 12%, respectively. Element-specific spatial distribution maps along the [001] direction of the $L1_2$-ordered γ′ phase reveal that both Mo and Cr preferentially replace Ti on its sublattice. The remaining excess Ti is available for formation of additional γ′, resulting in enhanced γ′ volume fractions.

The discovery of a γ/γ′ microstructure in the Co-Al-W system, i.e. cuboidal $L1_2$-ordered $Co_3(Al,W)$ precipitates formed in a disordered fcc Co matrix, similar to Ni_3Al in the Ni-Al system, has opened new pathways for developing Co-based high-temperature alloys [1–3]. These materials show remarkable properties such as high solidus and liquidus temperatures [4], positive γ/γ′ lattice misfit [5], and large processing windows for heat treatments and thermo-mechanical processing.

However, the two-phase γ/γ′ microstructure in Co-Al-W is reported to be metastable and known to form only within a narrow compositional range [2,6]. Equilibrium phases, e.g. B2-ordered CoAl and DO_{19}-ordered Co_3W [7], can lead to a significant deterioration of mechanical properties [8]. From an engineering point-of-view, Co-Al-W alloys are not favorable for jet-engine applications due to the large amount of W required for the stabilization of γ′ precipitates and the resulting high mass density [9–11]. Stabilization of γ′ without W addition has been recently demonstrated by combined alloying of Mo/Nb [12,13] and/or Mo/Ta [14] to the Co-Al system, yielding reduced mass density. However, the γ′ phase is reported to be metastable similar to $Co_3(Al,W)$ [9].

Co-Ti is reported to be the only binary Co-based system which forms thermodynamically stable γ′ (Co_3Ti) [15] and thus, Co-Ti-based alloys are promising alternatives to Co-Al-W alloys [10,16]. γ′ precipitates formed in the Co-Ti system give rise to substantial precipitation-hardening, similar to Ni-based superalloys [17,18]. The yield strength of Co_3Ti increases with increasing temperature above 200 °C and reaches a maximum between 700 and 800 °C [19,20], thus rendering Co_3Ti an appropriate reinforcement phase at elevated temperatures. However, binary Co-Ti alloys aged at 900 °C for 100 h exhibit only a low γ′ volume fraction of about 20% due to a high solubility of Ti (~10 at.%) in fcc-Co at 900 °C [21,22]. Moreover, γ′ precipitates are prone to coarsening when exposed to high temperatures due to a γ/γ′ lattice misfit ranging from 0.75 to 1.36% [10]. In order to overcome these drawbacks, systematic studies of the effects of alloying elements on the microstructure and properties of Co-Ti-based alloys are needed. Here, we report on the effect of Mo and Cr addition to a reference Co-Ti binary alloy with the aim of increasing the γ′ volume fraction and solvus temperature and optimizing the γ/γ′ lattice misfit. We provide quantitative data on elemental partitioning, elucidate the γ′ site-occupancy behavior of the solutes by means of atom probe tomography (APT) and discuss the observed microstructures based on the APT data.

Co-12Ti, Co-12Ti-4Mo, and Co-12Ti-4Cr (in at.%) alloys were cast and re-melted at least five times using the vacuum arc re-melting (VAR) process. The as-cast alloys were homogenized between 1150 and 1160 °C for 120 h and aged at 800 °C for 24 h. For all the heat treatments, the alloys were encapsulated in quartz tubes back-filled with Ar gas. The microstructures of the aged samples were characterized by backscatter electron (BSE) imaging in a scanning electron microscope (SEM) (Zeiss Merlin). Lattice misfit values of aged samples were measured by X-ray diffraction (XRD) (RIGAKU SmartLab) using CuKα1 radiation. Detailed scans of {111} Bragg reflections were performed in the angular range from 42 to 45° at a step size of 0.02 or 0.01 and scan rate of 0.3°/min or 0.1°/min. The {111}-reflections were fitted with two Pseudo-Voigt functions and lattice parameters of γ and γ′ were obtained after deconvolution of the overlapped functions. Phase transition temperatures of aged samples were determined by differential scanning calorimetry (DSC) (NETZSCH DSC 404C). DSC measurements were

* Corresponding author.
E-mail address: p.choi@kaist.ac.kr (P.-P. Choi).

https://doi.org/10.1016/j.scriptamat.2018.05.041
1359-6462/

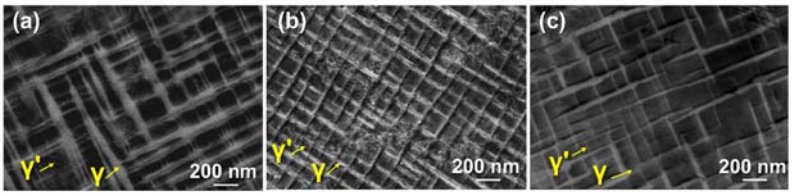

Fig. 1. BSE images of (a) Co-12Ti, (b) Co-12Ti-4Mo, and (c) Co-12Ti-4Cr after aging at 800 °C for 24 h. BSE: Back scattered electrons.

performed from room temperature to 1450 °C at a heating rate of 10 °C/min. To accurately resolve [001] lattice planes in APT analyses, grains with [001] orientation were identified using electron backscatter diffraction (EBSD). Wedge-shaped bars were cut and lifted out from those grains using a dual beam focused-ion-beam (FIB) instrument (Helios NanoLab 600i). The bars were attached to commercial flat-top Si micro tips and subsequently ion-milled into needle-shaped APT specimens according to the procedure described in Ref. [23]. The specimens were cleaned by a final step at a 5 kV acceleration voltage at a current of 41 pA to remove the regions severely damaged by Ga implantation. APT analyses were performed using a CAMECA LEAP™ 5000XS system in laser pulsing mode at a specimen base temperature of 40 K. A laser pulse frequency of 200 kHz and a pulse energy of 40 pJ were applied. Data analysis was performed with the software IVAS™ 3.6.14.

Fig. 1(a)–(c) shows BSE images of the aged Co-12Ti, Co-12Ti-4Mo, and Co-12Ti-4Cr samples. Two-phase γ/γ′ microstructures can be clearly observed for all three alloys. The γ channels and γ′ precipitates show bright and dark contrast, respectively, because of the difference in the average atomic number. [24,25]. The γ′ precipitates in the binary Co-12Ti alloy (Fig. 1(a)) are plate-shaped rather than cubic with an average length of 82 ± 12 nm. Such a precipitate morphology suggests that the γ/γ′ interfaces of the Co-12Ti alloy might be semi-coherent [26]. Using X-ray diffraction, we measured a γ/γ′ lattice misfit value of 1.17% for the Co-12Ti alloys (see Fig. S1 in Supplementary material), which is in good agreement with previous reports [10]. The relatively large lattice misfit favors the development of plate-shaped γ′ over cubic γ′ during aging at 800 °C. Aging at higher temperature for longer time, e.g. at 900 °C for 100 h, results in an irregular morphology, as reported by Zenk et al. [21]. Such a drastic change in γ′ morphology with varying aging conditions suggests that Co_3Ti precipitates are prone to coarsening.

Fig. 1(b) and (c) shows that two-phase γ/γ′ microstructures can also be observed for the aged Co-12Ti-4Mo and Co-12Ti-4Cr alloys, where these two ternary alloys exhibit nearly cubic γ′ precipitates. The measured lattice misfit values of Co-12Ti-4Mo and Co-12Ti-4Cr were 1.01% (Fig. S2) and 0.35% (Fig. S3), respectively, and hence lower than for Co-12Ti. The decrease in lattice misfit upon alloying with Mo and Cr is in agreement with the observed changes in γ′ morphology.

Fig. 2(a)–(c) shows proximity histograms [27] across the γ/γ′ interfaces of Co-12Ti, Co-12Ti-4Mo, and Co-12Ti-4Cr alloys, respectively. The proximity histograms reveal that Co and Cr partition to the γ phase, whereas Ti and Mo partition to the γ′ phase, in agreement with recent observations by Zenk et al. [10]. Individual γ and γ′ phase regions were selected from the APT datasets to determine the phase compositions directly from the corresponding mass spectra. The respective compositions of γ and γ′, elemental partitioning coefficients ($K_i = C_i^{\gamma}/C_i^{\gamma'}$), γ′ volume fractions, and phase transition temperatures are listed in Table 1. In the binary Co-12Ti alloy, Co partitions to γ and Ti to γ′. The Ti concentration in γ′ is 20.2 ± 0.1 at.% and thus deviates from the expected stoichiometry of the Co_3Ti phase. This experimental finding suggests the existence of anti-site defects in γ′, where excess Co atoms occupy Ti-sublattice sites. Such an assumption is in line with studies of single phase Co_3Ti, reported to exist in the range from 20 to 25 at.% Ti

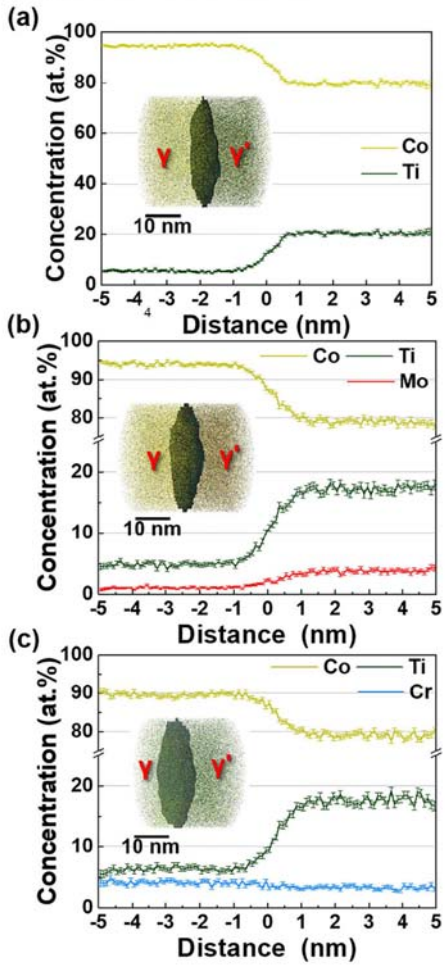

Fig. 2. Proximity histograms across γ/γ′ interfaces of (a) Co-12Ti (12.65 at.% Ti isoconcentration surface is the chosen reference γ/γ′ interface), (b) Co-12Ti-4Mo (10.36 at.% Ti isoconcentration surface) and (c) Co-12Ti-4Cr (10.67 at.% Ti isoconcentration surface) alloys.

Table 1
γ′/γ phase compositions, partitioning coefficients, γ′ volume fractions and phase transition temperatures for Co-12Ti, Co-12Ti-4Mo and Co-12Ti-4Cr alloys.

Alloys		Co-12Ti	+4Mo	+4Cr
γ′/γ concentration (at.%)	Co	79.8/93.6	79.1/93.8	79.6/88.9
	Ti	20.2/6.4	16.4/4.9	17.1/6.6
	Ternary	–	4.5/1.2	3.4/4.5
Partitioning coefficients ($K_x = C_x^{\gamma'}/C_x^{\gamma}$)	Co	0.9	0.8	0.9
	Ti	3.2	3.3	2.6
	Ternary	–	3.7	0.8
γ′ vol. fraction (%)		40.7	65.3	51.8
$T_{\gamma' \text{ solvus}}$ (°C)		1005	1119	1062
T_{Solidus} (°C)		1219	1193	1205
T_{Liquidus} (°C)		1318	1290	1321

due to partial substitution of Ti by Co [28,29]. In Co-12Ti-4Mo, Mo strongly partitions to the γ′ phase, whereas, in Co-12Ti-4Cr, Cr weakly partitions to the γ matrix (compare partitioning coefficients in Table 1).

Using the lever rule, the γ′ volume fractions can be estimated from the phase composition values (for lever rule plot see Fig. S4) [8]. The lever rule can be simply applied to the samples studied herein, since they all exhibit two-phase γ/γ′ microstructures. No other phases can be observed even at grain boundaries (see Fig. S5, Supplementary information). The measured γ′ volume fraction in binary Co-12Ti is ~40.7%, and it increases to 65.3% and 51.8% with the addition of Mo and Cr respectively. The γ′ volume fraction of the Co-12Ti-4Mo alloy is close to the optimum value required for high-temperature creep resistance of γ/γ′-strengthened Ni-based superalloys [30,31]. In addition, the measured γ′ solvus temperature of Co-12Ti-4Mo is 1119 °C and thus substantially higher than the γ′ solvus temperature of binary Co-12Ti (1005 °C) and of Co-9.2Al-9W (990 °C) (Fig. S6, Supplementary information) [2]. However, both solidus and liquidus temperatures of γ′ decrease with Mo addition. The Co-12Ti-4Cr alloy also exhibits an increased γ′ solvus temperature of 1062 °C but this increase is smaller than that of Co-12Ti-4Mo. Overall, we observe an increased thermal stability of γ′ with the addition of Cr and Mo to the Co-12Ti binary.

Fig. 3(a) shows a cumulative histogram of the ion impact positions on the position-sensitive detector of the APT instrument, i.e. field desorption map, acquired from the analysis of a Co-12Ti specimen. We can clearly identify a [001] pole (showing four-fold symmetry) nearly parallel to the tip axis, as expected from the EBSD-guided specimen preparation. Fig. 3(b) presents the corresponding APT reconstruction (yellow green: Co atom, dark green: Ti atom). The γ/γ′ interfaces are highlighted by Ti isoconcentration surfaces encompassing regions of ≥12.65 at.% Ti. A subset of this point cloud across this interface, shown in Fig. 3(c), reveals resolved lattice planes in both γ and γ′ along the [001] direction. Ti atoms occupy every second plane in γ′ as marked by red arrows. Element-specific spatial distribution maps (SDMs) [32] can be calculated along a specific orientation within the reconstructed dataset and they can be used to detect site-occupancy in ordered structures [33]. SDMs were acquired in the γ and γ′ phase along the [001] direction, as shown in Fig. 3(d). Within γ, SDMs for Co and Ti exhibit peaks at an average interspacing of approximately 0.18 nm [23]. It can be concluded that Co and Ti atoms are randomly distributed within this disordered γ phase. In contrast, the SDM for Co in γ′ reveals alternating high and low peaks every 0.18 nm, whereas for Ti, peaks appear at an average distance of 0.36 nm [23,34]. These findings give clear evidence for $L1_2$-type ordering of Co and Ti.

Fig. 4 shows SDMs calculated along the [001] direction in γ′ for both Co-12Ti-4Mo and Co-12Ti-4Cr. Mo shows periodic peaks with an average interspacing of about 0.36 nm identical to Ti (Fig. 4(a)), indicating that Mo occupies the Ti-sublattice sites in γ′ [35]. This observation is consistent with the measured drop in the Ti concentration in γ′ from 20.2% to 16.4% (see Table 1). Furthermore, the solubility of Ti in γ appears to be reduced by the addition of Mo to the binary alloy, as the Ti concentration in aged Co-12Ti-4Mo is 4.9 at.% Ti, as compared to 6.4 at.% Ti in aged Co-12Ti. Overall, Mo increases the partitioning coefficient of Ti (compare values for Co-Ti and Co-Ti-Mo in Table 1). As Ti has a strong tendency to partition to γ′, excess Ti resulting from partial substitution of Ti by Mo in γ′ contributes to the formation of additional γ′. We conclude that strong partitioning of Mo to γ′ and its tendency to occupy the Ti-sublattice within γ′ as well as a reduced Ti solubility in γ are

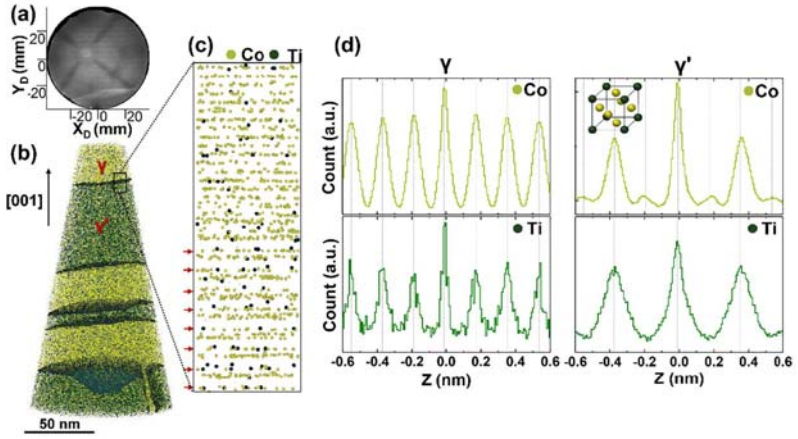

Fig. 3. (a) Field desorption map acquired from an APT analysis of a Co-12Ti sample. (b) APT reconstruction of the tip aligned along the [001] direction. γ/γ′ interfaces are highlighted by 12.65 at.% Ti isoconcentration surfaces. (c) Resolved [001] lattice planes in γ and γ′ phases across the interface. Lattice planes preferentially occupied by Ti atoms are marked with red arrows. (d) Spatial distribution maps (SDMs) of Co and Ti in γ and γ′ phases along the [001] direction. A schematic of the $L1_2$-ordered unit cell (yellow green: Co atom, dark green: Ti atom) was added as an inset to the SDM of Co in γ′. (For interpretation of the references to color in this figure legend, the reader is referred to the web version of this article.)

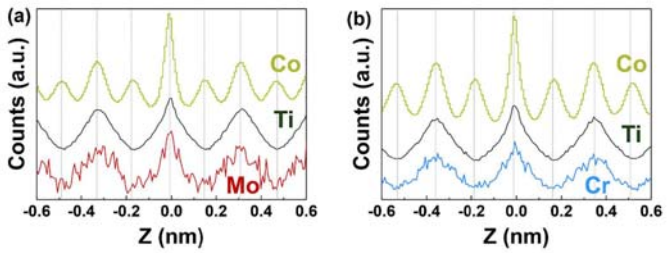

Fig. 4. Elemental SDMs along the [001] direction in γ′ for (a) Co-12Ti-4Mo and (b) Co-12Ti-4Cr along the [001] direction.

the key factors for the observed increase in the γ′ volume fraction upon alloying with Mo.

Fig. 4(b) shows SDMs for Co, Cr and Ti in γ′ for the Co-12Ti-4Cr alloy, which are very similar to the SDMs obtained for the same elements in the Co-12Ti-4Mo alloy. The Ti concentration in γ′ decreases to 17.1% with the addition of Cr. Although Cr preferentially partitions to γ (see Table 1), Cr in γ′ substitutes mostly Ti, thus leading to an increase in γ′ volume fraction, by virtue of the same mechanism as for Mo. However, Cr strongly reduces the partitioning coefficient of Ti. As can be seen in Table 1, the solubility of Ti in γ is little affected by Cr, which leads to a modest increase in γ′ volume fraction for the Co-12Ti-4Cr alloy as compared to the reference Co-12Ti alloy.

In conclusion, our investigation showed that Co-12Ti, Co-12Ti-4Mo and Co-12Ti-4Cr alloys when aged at 800 °C for 24 h exhibit a γ/γ′ microstructure, with both Mo and Cr addition leading to an increase in the γ′ volume fraction and γ′ solvus temperature. Mo strongly partitions to γ′, acting like a typical γ′ stabilizer, which contrasts with Cr partitioning to γ. Elemental SDMs in the γ′ phase give strong evidence that Mo and Cr occupy Ti sites in the $L1_2$-ordered structure, which, in turn, results in an increase in the γ′ volume fraction. The atomic-scale insights gained from our studies can be exploited for designing more advanced γ/γ′-strengthened Co-Ti based superalloys with superior γ′ phase stability and high temperature properties. We also consider the data presented herein as highly relevant for understanding the atomic-scale mechanisms and kinetics of γ′ precipitation in Co-Ti-based systems as a function of alloy composition. These issues will be addressed in a future study.

Acknowledgements

This work was supported by the National Research Foundation of Korea (NRF) [grant number 2016R1A2B4012426]; the U.S. Air Force Office of Scientific Research (AFOSR) [grant number FA2386-16-1-4120]. HI acknowledges financial support of R&E Initiative for Emerging Materials-based Creative Convergence. HI, SKM, BG, DR are grateful to U. Tezins and A. Sturm for their technical support of the atom probe tomography and focused ion beam facilities at the Max-Planck-Institut für Eisenforschung. SKM also acknowledges financial support from the Alexander von Humboldt Foundation.

Appendix A. Supplementary data

Supplementary data to this article can be found online at https://doi.org/10.1016/j.scriptamat.2018.05.041.

References

[1] C.S. Lee, Precipitation-hardening Characteristics of Ternary Cobalt-aluminum-X Alloys, (Ph.D. Thesis) The University of Arizona, Arizona, USA, 1971.
[2] J. Sato, T. Omori, K. Oikawa, I. Ohnuma, R. Kainuma, K. Ishida, Science 312 (2006) 90.
[3] S. Meher, H.Y. Yan, S. Nag, D. Dye, R. Banerjee, Scr. Mater. 67 (2012) 850.
[4] T.M. Pollock, J. Dibbern, M. Tsunekane, J. Zhu, A. Suzuki, JOM 62 (2010) 58.
[5] H. Mughrabi, Acta Mater. 81 (2014) 21.
[6] S. Kobayashi, Y. Tsukamoto, T. Takasugi, H. Chinen, T. Omori, K. Ishida, S. Zaefferer, Intermetallics 17 (2009) 1085.
[7] S. Kobayashi, Y. Tsukamoto, T. Takasugi, Intermetallics 31 (2012) 94.
[8] I. Povstugar, P.P. Choi, S. Neumeier, A. Bauer, C.H. Zenk, M. Göken, D. Raabe, Acta Mater. 78 (2014) 78.
[9] S.K. Makineni, B. Nithin, D. Palanisamy, K. Chattopadhyay, J. Mater. Sci. 51 (2016) 7843.
[10] C.H. Zenk, I. Povstugar, R. Li, F. Rinaldi, S. Neumeier, D. Raabe, M. Göken, Acta Mater. 135 (2017) 244.
[11] I. Povstugar, C.H. Zenk, R. Li, P.-P. Choi, S. Neumeier, O. Dolotko, M. Hoelzel, M. Göken, D. Raabe, Mater. Sci. Technol. 32 (2016) 220.
[12] S.K. Makineni, B. Nithin, K. Chattopadhyay, Scr. Mater. 98 (2015) 36.
[13] S.K. Makineni, B. Nithin, K. Chattopadhyay, Acta Mater. 85 (2015) 85.
[14] S.K. Makineni, A. Samanta, T. Rojhirunsakool, T. Alam, B. Nithin, A.K. Singh, R. Banerjee, K. Chattopadhyay, Acta Mater. 97 (2015) 29.
[15] M. Jiang, G. Saren, S.Y. Yang, H.X. Li, S.M. Hao, Trans. Nonferrous Metals Soc. China 21 (2011) 2391.
[16] J.J. Ruan, X.J. Liu, S.Y. Yang, W.W. Xu, T. Omori, T. Yang, B. Deng, H.X. Jiang, C.P. Wang, R. Kainuma, K. Ishida, Intermetallics 92 (2018) 126.
[17] T. Takasugi, S. Hirakawa, O. Izumi, S. Ono, S. Watanabe, Acta Metall. 35 (1987) 2015.
[18] T. Takasugi, O. Izumi, Acta Metall. 33 (1985) 39.
[19] T. Takasugi, O. Izumi, Acta Metall. 34 (1986) 607.
[20] Y. Liu, T. Takasugi, O. Izumi, H. Suenaga, J. Mater. Sci. 24 (1989) 4458.
[21] C.H. Zenk, S. Neumeier, H.J. Stone, M. Göken, Intermetallics 55 (2014) 28.
[22] T. Takayama, M.Y. Wey, T. Nishizawa, Trans. Jpn. Inst. Metals 22 (1981) 315.
[23] S. Meher, P. Nandwana, T. Rojhirunsakool, J. Tiley, R. Banerjee, Ultramicroscopy 148 (2015) 67.
[24] G.E. Lloyd, Mineral. Mag. 51 (1987) 3.
[25] C.H. Zenk, S. Neumeier, N.M. Engl, S.G. Fries, O. Dolotko, M. Weiser, S. Virtanen, M. Göken, Scr. Mater. 112 (2016) 83.
[26] J.M. Howe, H.I. Aaronson, R. Gronsky, Acta Metall. 33 (1985) 639.
[27] O.C. Hellman, J.A. Vandenbroucke, J. Rüsing, D. Isheim, D.N. Seidman, Microsc. Microanal. 6 (2000) 437.
[28] T. Takasugi, O. Izumi, Acta Metall. 33 (1985) 33.
[29] T. Shinohara, T. Takasugi, H. Yamauchi, T. Kamiyama, H. Yamamoto, O. Izumi, J. Phys. F: Met. Phys. 16 (1986) 1845.
[30] Y. Ro, Y. Koizumi, H. Harada, Mater. Sci. Eng. A 223 (1997) 59.
[31] T. Murakumo, Y. Koizumi, K. Kobayashi, H. Harada, in: K.A. Green, et al., (Eds.), Superalloys, TMS, Warrendale, PA 2004, pp. 155–162.
[32] B.P. Geiser, T.F. Kelly, D.J. Larson, J. Schneir, J.P. Roberts, Microsc. Microanal. 13 (2007) 437.
[33] B. Gault, X.Y. Cui, M.P. Moody, F.D. Geuser, C. Sigli, S.P. Ringer, A. Deschamps, Scr. Mater. 66 (2012) 903.
[34] Q. Yao, H. Xing, J. Sun, Appl. Phys. Lett. 89 (2006) 161906.
[35] S. Meher, R. Banerjee, Intermetallics 49 (2014) 138.